Enhancement of Photoelectrochemical Hydrogen Production from Hematite Thin Flms by the Introduction of Ti and Si

4 AUTHORS, INCLUDING:

Julie Anne Glasscock
Kadagaya Project
33 PUBLICATIONS   790 CITATIONS

SEE PROFILE

Piers R. F. Barnes
Imperial College London
79 PUBLICATIONS   3,487 CITATIONS

SEE PROFILE

Enhancement of Photoelectrochemical Hydrogen Production from Hematite Thin Films by the Introduction of Ti and Si

Julie A. Glasscock,* Piers R. F. Barnes, Ian C. Plumb, and Nick Savvides

CSIRO Materials Science and Engineering, P.O. Box 218, Lindfield NSW 2070, Australia

Received: June 12, 2007; In Final Form: August 28, 2007

Doped and undoped hematite (α-Fe_2O_3) thin film electrodes for photoelectrochemical hydrogen production have been prepared using reactive magnetron sputtering. We present an extensive characterization of the photoelectrochemical, structural, electrical, and optical properties of the α-Fe_2O_3 films to assess the mechanisms by which the dopants influence photoelectrode performance. The Si-doped and Ti-doped α-Fe_2O_3 exhibited much higher photoelectrochemical activity than the undoped material. The Ti-doped α-Fe_2O_3 showed the largest photocurrent as well as the lowest onset potential, the highest electrical conductivity, the lowest activation energy, and the highest charge carrier density. The crystallographic orientation of the films does not appear to be a dominant factor affecting the photocurrent. The changes in conductivity with doping are insufficient to explain the observed changes in the photoelectrochemical activity. The proposed mechanism for the enhanced photocurrent is reduction of recombination due to an improvement of the charge-transfer rate coefficient at the surface and also possibly passivation of the grain boundaries by the dopants. A highly disordered surface and higher grain boundary recombination due to small crystals may explain the lower photocurrent of the Si-doped α-Fe_2O_3 compared to the Ti-doped material.

1. Introduction

Several materials have been investigated as semiconducting catalyst materials for photoelectrochemical hydrogen production (water splitting).[1,2] Compared to other materials, hematite (α-Fe_2O_3) has the desired property of a narrow indirect band gap of approximately 2.2 eV (which in principle allows the utilization of a larger fraction of the solar spectrum than wider band gap semiconductors such as TiO_2), together with low cost, electrochemical stability, and low toxicity.[3−9] The reported water splitting efficiencies for α-Fe_2O_3 are much lower than the theoretical maximum efficiency for this material of 12.9%.[3] This is due to a number of factors including the falloff in the absorption cross-section of the material for wavelengths approaching the band gap value, the rapid electron−hole recombination in the semiconductor resulting in short diffusion lengths of charge carriers,[10] and slow surface reaction kinetics.[11] In addition, the conduction band edge of hematite is below that of the H^+/H_2 redox potential; hence, spontaneous water splitting is not possible, and an electrical bias must be applied to generate hydrogen.[12]

Doping of pure α-Fe_2O_3 has been extensively investigated in an attempt to yield improved photoelectrochemical performance. The majority of dopants have been shown to decrease the photocurrent,[9,13,14] but the introduction of both Ti[9,10,15] or Si[4,16−19] into α-Fe_2O_3 has achieved enhanced photoelectrochemical response of hematite electrodes. Jorand Sartoretti et al.[9] observed that doping α-Fe_2O_3 with around 5% of titanium increased 4-fold the photocurrent of films prepared by spray pyrolysis. They also found that the photocatalytic activity of the Ti-doped α-Fe_2O_3 was enhanced by the addition of 1% Al which they attributed to the formation of Al_2O_3 which is isostructural with hematite and thereby directed the crystallinity of the films. Early research into doping polycrystalline α-Fe_2O_3 powders with group IVA elements indicated that Si-doped material had higher photocurrents than hematite doped with Ti (group IVB element).[17,18] It was suggested that additional energy levels introduced by the Ti ion centers may be acting as recombination sites, leading to lower photocurrents.[17] The influence of the dopants on carrier mobility remains poorly understood due to uncertain contributions from grain boundary resistance in polycrystalline specimens,[20,21] difficulties linked to the magnetic susceptibility of α-Fe_2O_3 during Hall measurements[22] and uncertainty in impurity concentration and type.[23] The influence of Ti and Si dopants on thin film electrodes (where impurities could also affect film morphology) is even less well understood.

It has been suggested that the electrical conductivity of hematite influences the photoelectrochemical performance.[4,16] This is because a substantial potential drop is expected during the transport of photoelectrons through the bulk of the electrode in high resistance materials. High purity hematite has a very low conductivity, and doping has been shown to increase the conductivity for single crystal and bulk polycrystalline electrode samples.[20,21,23−26] It has been proposed that in general the impurities are not the actual donors or acceptors, but they are charge compensated by the parent ions with different valences as shown in eq 1 for the case of Ti-doping.[27] This results in enhanced conductivity via the small polaron hopping mechanism.[23,28−30]

$$Fe^{3+} + Ti^{3+} \rightarrow Fe^{2+} + Ti^{4+} \tag{1}$$
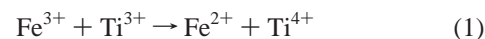
However, even for a resistive ($\rho \sim 10^5$ Ω cm) thin film (thickness $h \sim 1$ μm) photoelectrodes operating at the theoretical maximum photocurrent for solar illumination, assuming complete absorption and conversion of photons with energies exceeding the band gap (photocurrent density $j = 10.6$ mA

* To whom correspondence should be addressed. Tel: +61 (0)2 9413 7173. Fax: +61 (0)2 9413 7200. E-mail: Julie.Glasscock@csiro.au.
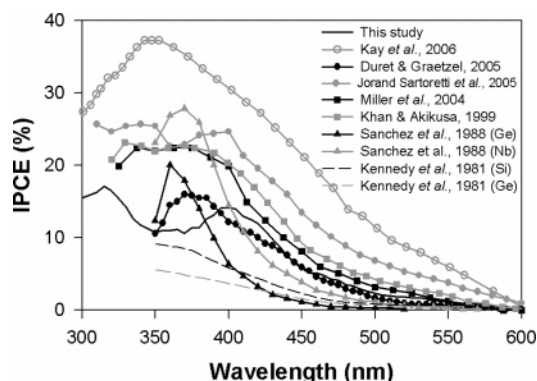
Figure 1. Comparison of incident photon-to-electron conversion efficiencies (IPCE) as a function of wavelength as presented in the literature (see Table 1 for sample and measurement details).

cm^{-2}), there will only be a modest drop in potential ($j_p\rho h \leq$ 100 mV). In practice lower photocurrent densities are obtained with correspondingly lower potential drops, such that ohmic potential drops due to photoelectrode resistivity have only a minor direct influence on thin film performance. Thus lowering ohmic voltage drops in the electrode by increasing conductivity cannot alone explain the large improvements due to doping. Also, changes in conductivity should not shift the onset potential of the material.

An approach to improve conversion efficiency is by combating the effect of the reported short diffusion length of charge carriers (2−4 nm)[10] through introducing a nanometer scale structure to a hematite film. Hematite has been nanostructured to produce well-aligned nanowires by aqueous chemical growth[31,32] and by thermal oxidation of iron foil[33−37] and to produce dendritic nanostructures using atmospheric pressure CVD and spray pyrolysis.[4,16] Beermann et al.[31] showed that undoped nanorod arrays of α-Fe$_2$O$_3$ exhibit higher photocurrents than nanoparticulate films. This difference was attributed to a greater number of grain boundaries in nanoparticulate films which act as recombination sites for charge carriers. Kay et al.[4] and Cesar et al.[16] observed high photocurrents from Si-doped dendritic nanostructured films. The formation of nanostructures was attributed to the structure-directing behavior of Si, producing a film with preferred crystallographic orientation. It was claimed that the Si also acts as a dopant, increasing the electrical conductivity. However, it was not clear whether the doping, crystalline alignment, or nanostructuring was the dominant factor contributing to the observed improvement in photocurrent.

Apart from the most recent results reported by Kay et al.,[4] the incident photon-to-electron conversion efficiencies (IPCE) of nanostructured electrodes reported to date are not substantially better than those previously reported for solid polycrystalline or single-crystal specimens (see literature IPCE data compiled in Figure 1 with corresponding preparation and measurement details given in Table 1). This brings into focus the question of the relative importance of nanostructuring and morphology versus the modification of the electronic properties or the catalytic properties of the α-Fe$_2$O$_3$ surface by dopants. Improved understanding of the role of these factors in hematite photoelectrodes will be necessary before informed progress can be made. It is interesting to observe that the majority of the IPCE curves shown in Figure 1 exhibit photoactivity well beyond the notional cutoff wavelength (564 nm) for a material with a band gap of 2.2 eV.

In this study, we investigate the effect of doping with Ti or Si on the properties of thin films of hematite deposited by reactive magnetron sputtering. Undoped α-Fe$_2$O$_3$ films have

been fabricated using magnetron sputtering for photoelectrochemical applications.[38] However, we are not aware of any studies where magnetron sputtered hematite has been doped, for hydrogen production or other applications. We present a thorough characterization of the photoelectrochemical, structural, electrical, and optical properties of our doped and undoped α-Fe$_2$O$_3$ films to assess the mechanisms by which these impurities influence photoelectrode performance. Once the role of dopants in enhancing the photoelectrochemical activity of hematite thin films has been investigated, these films will be deposited onto nanostructured substrates[39] to examine independently the role of nanostructuring on the electrode performance.

2. Experimental Section

Film Preparation. The hematite thin films were deposited using a reactive DC magnetron sputtering system described in detail elsewhere.[43] This system used alloyed sputtering targets in order to incorporate the dopant. As a result, the dopant concentration was not easily varied, and therefore, dopant concentrations (and the purity levels) of the iron targets were selected after considering previous studies of the effects of dopants and impurities on the photoelectrochemical and electrical properties of hematite.[12,17,27] For depositing pure, Ti-doped and Si-doped α-Fe$_2$O$_3$ respectively, the following sputtering targets were used: 99.95% Fe, Fe with 5 at. % Ti and transformer steel (Fe with around 5 wt % Si and <1 wt % Al). Oxygen was the major impurity in the 99.95% Fe target with all other impurities in the parts-per-million range. Lower fractions of Si-dopant (<2%) have generally been incorporated into α-Fe$_2$O$_3$,[4,17] though up to 10% has been used.[19] The presence of around 1% Al in this alloy may also be beneficial to the doping process (as observed by Jorand Sartoretti et al.).[9]

The deposition of the α-Fe$_2$O$_3$ films using the reactive magnetron sputtering system was undertaken in a vacuum chamber evacuated to a base pressure of 10^{-4} Pa. The substrates were heated to 300 °C using a heating coil within the substrate mounting block. The temperature of the substrates was measured using a thermocouple which was embedded in a copper block fixed to the substrate holder. The substrate was held at 300 °C for 1 h prior to deposition. The pure and doped iron targets (75 mm diameter) were sputtered in an atmosphere of 0.2 Pa of O$_2$ and 0.8 Pa of Ar. The magnetron was operated at a power of 100 W (~330 V and ~0.3 A). Under these conditions, films were deposited at an average rate of around 200 nm/h. Various substrates were used including fluorine-doped tin oxide (FTO) conducting glass (Pilkington TEC 15, 14 Ω/sq), quartz glass (Electron Microscopy Sciences, 1 mm thick), silicon (Silicon Wafer Enterprises N100 test wafer, 1−10 Ω /sq, 500 ± 50 μm thick), and titanium sheet (Aldrich, 99.7%, 0.25 mm thick, etched in Kroll's solution for 5 s). After deposition, the films were left to cool in the chamber. They were then moved to a furnace and annealed in air at 550 °C for 1 h (heated at rate of 10 °C/min from 250 °C, cooled from 550 °C to 200 °C over 1.5 h).

The conditions described above were found to give the highest photocurrent of those tested. Various deposition parameters were investigated in the optimization process, including lower oxygen partial pressure (0.1 Pa O$_2$ and 0.9 Pa Ar), lower temperature (higher temperatures were not achievable with the heating system), and lower magnetron power (to reduce the deposition rate). Reducing the oxygen pressure and temperature had a negative effect on the photocurrent of the films, while the lower deposition rate did not change the photocurrents.

Photoelectrochemistry. The photoelectrochemical performance of the hematite thin films was measured using a standard

Enhanced Hydrogen Production from Doped Hematite

J. Phys. Chem. C, Vol. 111, No. 44, 2007 **16479**

TABLE 1: Sample and Measurement Conditions for Literature IPCE Results Shown in Figure 1[a]

author	sample	dopant	potential (V/RHE)
this study	sputtered,polycrystalline film	Ti	1.5
Kay et al., 2006[4]	ultrasonic spray pyrolysis and CVD,nanostructured	Si	1.23
Duret and Grätzel, 2005[40]	spray pyrolysis,nanostructured	Si[†]	1.2
Jorand Sartoretti et al., 2005[9]	spray pyrolysis,polycrystalline film	5% Ti + 1% Al	1.47*
Khan and Akikusa, 1999[41]	single crystal		1.43*
Sanchez et al., 1988[42]	single crystal	Ge, Nb	1.07*
Miller et al., 2004[38]	sputtered,polycrystalline film		1.27*
Kennedy et al., 1981[17]	sintered powder polycrystalline	Si, Ge	1.28*, 1.23*

[a] Jorand Sartoretti et al., used an electrolyte of 0.1 M NaOH, all others used 1 M NaOH. *Potential converted from another reference potential.
[†] Data presented as undoped, reported in a later publication[16] that samples were unintentionally doped with Si.

three-electrode photoelectrochemical cell fitted with a quartz window, illuminated using a 1000 W xenon arc lamp fitted with a water filter and has been described in detail elsewhere.[3] The three electrodes were the working electrode (the hematite thin film), a platinum-wire counter electrode, and a saturated calomel reference electrode (SCE). The electrodes were immersed in 1 M NaOH electrolyte. Photocurrent density, j_p, as a function of bias potential, V (vs SCE), was determined from the difference between the stable current measured under illumination (80 mW cm^{-2}) and the current in the dark. Photocurrent transients were observed by chopping the light source during a 20 mV/s scan of the bias potential/SCE. The IPCE was measured by passing the output from the xenon lamp through a 12 nm band-pass monochromator and measuring the photocurrent as a function of wavelength over the range 250−650 nm. A 435 nm cutoff filter was introduced for scans at wavelengths exceeding 500 nm to eliminate artifacts from second-order diffraction. The irradiances over the same wavelength range were measured using a thermopile and the IPCE calculated using eq 2 where $I(\lambda)$ is the incident photon flux passed by the monochromator when set to wavelength λ and e is the electronic charge.

$$IPCE(\lambda) = j_p(\lambda)/[eI(\lambda)] \qquad (2)$$

Optical Measurements. Direct transmittance (T) and specular reflectance (R) measurements were made over a wavelength range of 250−2000 nm using a Cary5 spectrophotometer. Reflectance measurements used a $V-W$ (double reflection) attachment calibrated using gold and silicon reference surfaces. The spectrophotometer data at wavelengths below the band gap value (<564 nm) were fitted by a Cauchy model[44] using WVASE software (WVASE32 TM, J.A. Woollam Co. Inc.) to determine the refractive index n, extinction coefficient κ, and film thickness for films deposited both on FTO glass and quartz glass. The absorption coefficient α was calculated from the extinction coefficient using eq 3. The FTO glass substrates were modeled using a multilayer Drude Lorenz oscillator model (WVASE). Additionally, the optical constants at more strongly absorbing wavelengths for films on quartz substrates were calculated explicitly with a numerical solver using a modification of the formulation of Szczyrbowski[45] described in more detail in a previous publication.[46]

$$\alpha = 4\pi\kappa/\lambda \qquad (3)$$

Structural Measurements. Raman spectroscopy was undertaken using a Renishaw inVia system. The laser beam ($\lambda = 514.5$ nm) was focused on the sample by a lens to yield a spot with a diameter of approximately 2 μm. A laser power of 1.36 mW was chosen, which was previously determined to be low enough not to degrade the samples.[46] Spectra were measured over a range of wavenumbers from 100 to 2000 cm^{-1} (5−100

μm). The acquisition time was 10 s, and ten measurements were averaged to increase the signal-to-noise ratio.

The crystalline structure of the α-Fe$_2$O$_3$ films was analyzed using a PANalytical X'Pert PRO $\theta - 2\theta$ diffractometer with a Cu Kα source, over an angular range of $2\theta = 10-80°$. The morphology of the films was examined using a dual-beam FEI Nova scanning electron microscope (SEM) equipped with a Ga ion source for focused ion beam milling. Trenches were milled into the samples perpendicular to the surface and the resulting cross-sections imaged at 52° to the perpendicular. Film thicknesses were determined from the SEM images and compared to the thicknesses derived from optical measurements. Energy dispersive X-ray spectroscopy (EDS) was undertaken using an Oxford Instruments system integrated into a JEOL 5400 electron microscope in order to identify and quantify the dopants in the films.

Electrical Measurements. Resistivity measurements were undertaken using specifically prepared substrates. A strip of the FTO film around 4 mm wide was removed from the center of the conducting glass substrate (40 mm × 10 mm) by etching with Zn powder and fuming (37%) hydrochloric acid to create two isolated pads of conducting film each about 18 mm × 10 mm. The substrate was masked at both ends before deposition (to leave areas clear for making contacts), resulting in a central area of α-Fe$_2$O$_3$ film (20 mm × 10 mm). Metal clips were used to make contact with the conducting glass. Lateral conductivity measurements of the films were made in air (50% humidity at 294 K) and in argon gas as a function of temperature (294−460 K) by measuring the current as a function of applied potential between the coplanar FTO contacts.

Electrochemical impedance spectroscopy measurements were made using a potentiostat (Radiometer Analytical VoltaLab PGZ 301) in conjunction with the electrochemical cell described above. The d.c. potential of the working electrode was stepped between −0.9 and +0.8 V vs SCE (100 mV increments) with a 20 mV a.c. signal superimposed to make the impedance measurement at frequencies between 100 kHz and 2.5 Hz (with 10 frequencies per decade). Data from the higher frequency range (where the influence of the Helmholtz layer and surface states can be neglected)[47] were used to determine the capacitance, C, of the space charge layer at the semiconductor−electrolyte interface by fitting a simple series-parallel RC equivalent circuit to the impedance values using a nonlinear least-squares routine. The cell impedance in the chosen frequency range was modeled using eq 4 at each applied potential, where R_s is the series resistance of the cell, R_p is the resistance of the space charge layer, and ω is the angular frequency of the measurement.

$$Z = R_s + (i\omega C + R_p^{-1})^{-1} \qquad (4)$$

The values of $C(V)$ were then used to determine the flat-band potential, V_{fb}, and the conduction electron concentration, N_D, of the Fe_2O_3 of the films using the Mott−Schottky relationship (eq 5), where A is the surface area of the electrode, ϵ_r is the dielectric constant of hematite (taken as 24),[11] ϵ_0 is the permittivity of free space, k is Boltzmann's constant, and T is the temperature. The uncertainty range on these measurements was estimated by calculating the spread of N_D and V_{fb} values determined from the Mott−Schottky plots at single frequencies within the fitted frequency range. We note that values determined at lower frequencies than the fitting range yielded substantially higher N_D values and more positive V_{fb} values as the capacitance increased, probably due to surface states.

$$(A/C)^2 = 2(eN_D\epsilon_r\epsilon_0)^{-1}(|V - V_{fb}| - kT/e) \quad (5)$$

Models of the lower frequency impedance of semiconductor electrodes can be extremely complicated, incorporating an array of circuit elements.[48,49] In an effort to approximately determine the concentration of surface states per unit potential, N_{ss}, and the time constant, τ, for emission and capture of electrons by the states, we made the simple assumption that the frequency-dependent residual capacitance eq 6 could be attributed predominantly to part of a continuum of electronic surface states at potential V within the band gap.[50]

$$C_{ss}(\omega) = C(\omega) - C \quad (6)$$

We fitted the residual capacitance due to surface states according to eq 7 at each measured potential[51] where the states become "frozen out" at high frequencies since τ is inversely proportional to the thermal velocity of electrons and the trap cross-section. This model is usually applied to electronic states at the interface of a semiconductor-metal Schottky junction.[52]

$$C_{ss}(\omega) = (N_{ss}e^2/\omega\tau) \arctan(\omega\tau) \quad (7)$$

3. Results

The reactive magnetron sputtering of all three targets produced orange-red α-Fe_2O_3 films which were transparent and adhered well to all of the substrates used. The Ti-doped α-Fe_2O_3 films deposited on silicon substrates exhibited some minor crazing. The films deposited at lower oxygen partial pressure (0.1 Pa O_2) were dark blue and reflective but changed color to orange-red after annealing. The dopant levels of the Ti-doped and Si-doped hematite films, as determined by quantitative EDS, were 5.0 ± 0.3 atomic % and 5.3 ± 0.3 atomic % respectively, which is in agreement with the composition of the targets, indicating that no significant preferential sputtering occurred.

Some of the characterization techniques required the hematite films to be deposited onto substrates other than conducting glass. A potential problem with measurements of this kind is that the properties of the α-Fe_2O_3 film (in particular, the crystallographic orientation) may differ. Differences in XRD relative peak heights were observed for hematite films deposited onto conducting glass, silicon, and silica substrates, consistent with small changes in crystallographic orientation. The results of the optical and electrical measurements reported below may therefore not be truly representative of the material deposited on the conducting glass.

Photoelectrochemistry. The photoelectrochemical performance of the doped and undoped α-Fe_2O_3 films was quantified by measuring the photocurrent density as a function of voltage vs the SCE reference electrode, as shown in Figure 2A. The
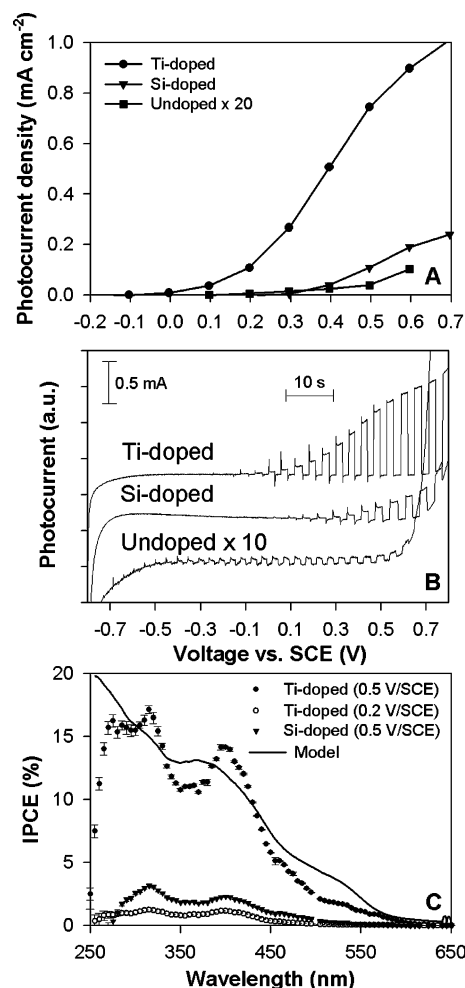

Figure 2. (A) Steady-state photocurrent density and (B) chopped light potential sweep (+20 mV/s) showing transient current relaxation of the doped and undoped α-Fe_2O_3 films as a function of voltage (V vs SCE) in 1 M NaOH, and (C) IPCE as a function of wavelength of the doped α-Fe_2O_3 films at 0.5 and 0.2 V vs SCE, with a Schottky barrier model[55] of the Ti-doped data at 0.5 V vs SCE.

undoped hematite shows a very small photocurrent (<1 μA cm^{-2} at 0.2 V vs SCE), with a steady-state onset potential of 0.1 V vs SCE (see Table 2). The steady-state onset potentials were inferred from the intercept ($j_p^2 = 0$) of the linear fit to j_p^2 against V.[53] The doped films exhibit higher photocurrents than the undoped material, with the Ti-doped α-Fe_2O_3 having the highest photocatalytic activity. Ti-doping resulted in a significant shift of the steady state onset potential to lower voltages (-0.15 V vs SCE). Films deposited at lower oxygen pressure (0.1 Pa O_2, 0.9 Pa Ar; results not shown) showed less than 5% of the photocurrent of those deposited using standard conditions of 0.2 Pa O_2, 0.8 Pa Ar.

It has been suggested that slow surface reaction kinetics enhance recombination at the surface of α-Fe_2O_3.[11] Therefore, a possible explanation for the enhanced photocurrent of Ti-doped hematite is that TiO_2 (known to be a good catalyst material) forms on the surface of the iron oxide and provides a catalytic function for the water splitting reaction. This hypothesis was tested by depositing very thin films (around 10 nm) of TiO_2 or Ti-doped α-Fe_2O_3 onto an undoped hematite film. The additional film was kept thin so that it did not contribute significantly to optical absorption but could provide catalytic functionality. No improvement in the photoelectrochemical properties of the undoped hematite was observed by the addition of either of these thin films.

Enhanced Hydrogen Production from Doped Hematite

J. Phys. Chem. C, Vol. 111, No. 44, 2007 **16481**

TABLE 2: Electrical Properties of Doped and Undoped α-Fe$_2$O$_3$ Films Determined from Electrical Conductivity and Electrochemical Impedance Spectroscopy

α-Fe$_2$O$_3$ electrode	σ_{295K} (Ω m)$^{-1}$	E_a (eV)	N_D (m^{-3})	V_{fb} (V/SCE)	μ (m^{2}s^{-1}V^{-1})	V_{onset} steady (V/SCE)	V_{onset} transient (V/SCE)	τ_1 (s)	τ_2 (s)
undoped	3×10^{-4}	0.68	$1.3^{+0.1}_{-0.7} \times 10^{24}$	$-0.84^{+0.02}_{-0.07}$	1×10^{-9}	0.10	-0.7	0.3	6
Si-doped	2×10^{-3}	0.34	$7.6^{+11}_{-0.3} \times 10^{24}$	$-0.69^{+0.12}_{-0.00}$	2×10^{-9}	0.20	-0.1	0.1	3
Ti-doped	5×10^{-2}	0.23	$3.3^{+1.4}_{-1.0} \times 10^{26}$	$-0.99^{+0.20}_{-0.01}$	1×10^{-9}	-0.15	-0.25	0.2	3

A reduction in deposition rate was investigated as good photocurrents have been reported for ultrasonic spray pyrolyzed α-Fe$_2$O$_3$ films deposited at a low deposition rate (<1 nm/min)[16] and our experience that films deposited using filtered arc deposition[46] at high deposition rates (70 nm/min) produced very small photocurrents. It should be noted, however, that the current state-of-the-art films produced by atmospheric CVD were deposited at a deposition rate of 100 nm/min.[4] The deposition rate scales approximately linearly with power, so a set of films was prepared at half of the standard power setting of the magnetron (i.e., at approximately half the deposition rate). The photocurrents generated by the Si-doped and Ti-doped α-Fe$_2$O$_3$ films deposited at half the magnetron power (lower deposition rate) did not show a significant change in photocurrent or onset potential relative to films of similar thickness deposited at the higher deposition rate.

Potential sweeps of the electrodes are shown under chopped illumination in Figure 2B. All films showed transients in the photocurrent, though these were small in the case of the undoped α-Fe$_2$O$_3$. The relaxation of the transient photocurrents for the electrodes were analyzed at a number of fixed potentials and were found to be composed of two relaxation processes, with time constants τ_1 and τ_2 (as shown in Table 2). The transient photocurrents (not shown) from which the time constants were calculated, were measured at a single potential for around 30 s following the cutoff of the radiation. The two time constants were determined by first fitting one exponential curve to the tail of the decay, subtracting this component, and then fitting the second additional exponential term to the beginning of the decay. The faster process had mean time constants of 0.20 ± 0.09 and 0.11 ± 0.03 s for the Ti-doped and Si-doped films, respectively, and 0.3 ± 0.2 s for the undoped film. The second slower relaxation time constant was approximately 3 s for the doped films and around 6 s for the undoped film. The chopped sweeps in Figure 2B were also used to determine the transient photocurrent onset potential which is thought to be closely related to the flat-band potential of the electrode.[11] As listed in Table 2, these values are -0.7, -0.1, and -0.25 V vs SCE for the undoped, Si-doped, and Ti-doped hematite films, respectively. Surprisingly, the undoped sample showed the most negative measurable transient onset, although it must be emphasized that the photocurrents for this sample are extremely small.

Action spectra (IPCE values as functions of wavelength) of the doped films, measured at potentials of 0.2 and 0.5 V vs SCE are shown in Figure 2C. The undoped film had a very small response at these potentials and is not shown. The Ti-doped film has a substantially higher response than the Si-doped film at all wavelengths. The drop-off in the IPCE at short wavelengths has been observed previously for hematite (see Figure 1) and other materials such as TiO$_2$[54]. The IPCE measurements for the Ti doped film in Figure 2C were analyzed by fitting a simple Schottky barrier model which assumes a solid film.[55] The absorption coefficient presented in Figure 3B was used to describe the absorption of radiation in the semiconductor after correction for surface reflectance.[3] Photoholes generated

within the depletion layer of the film are assumed to be rapidly transported to the electrode surface by the strong electric fields in this region, and a fraction of the holes generated in the bulk of the film are assumed to diffuse to the edge of the depletion layer where they are collected. Fits to a model allowing the hole diffusion length, surface transfer coefficient, and depletion layer width to vary are shown in Figure 2C. In the least-squares fit shown, the diffusion length is very small (<0.1 nm), so the modeled fit is scaled by the width of the depletion layer (3−5 nm) and the transfer coefficient (0.8−1). This barrier layer model does not describe the observed IPCE well. In particular, the modeled IPCE is noticeably higher than the measured values at long wavelengths, which may suggest that additional processes are involved which are not accounted for in the description. We are currently investigating this issue further.

Integrating the product of the IPCE, the photon flux of an illuminating spectrum, and the electronic charge over wavelength yields the expected photocurrent density generated by the film in broad band illumination if the photoresponse is assumed linear with intensity.[3] This photocurrent density can be compared with direct measurement under broad band illumination. At 0.5 V vs SCE the integrated photocurrent for the xenon lamp photon flux spectrum yields 0.62 mA cm^{-2} for the Ti-doped sample shown in Figure 2C, which is slightly lower than the directly measured 0.75 mA cm^{-2} at this potential. The discrepancy, which is of marginal statistical significance, could be due to nonlinearity of the electrode photoresponse. Similarly, the Si-doped sample yields an integrated photocurrent of 0.10 mA cm^{-2}, close to the measured value of 0.11 mA cm^{-2}. Performing the same integration using the solar AM 1.5 photon flux spectrum gives photocurrent densities of 0.57 and 0.10 mA cm^{-2} for the Ti− and Si-doped electrodes respectively at 0.5 V vs SCE.

In order to understand the differences observed in the photoelectrochemical behavior of the doped and undoped hematite, we undertook characterization of the film morphologies and crystal structures, and the electrical and optical properties.

Optical Properties. The optical constants (refractive index n and the extinction coefficient κ) determined from a 120 nm thick, Ti-doped α-Fe$_2$O$_3$ film are presented in Figure 3A over the wavelength range of 250−2000 nm. The absorption coefficient is shown in Figure 3B. Quantitative optical constants were derived only for a Ti-doped α-Fe$_2$O$_3$ film deposited on a quartz glass substrate. Reflectance and transmittance measurements of all three sample types (deposited on FTO conducting glass) were undertaken, which showed that, after allowance for differences in thickness, the optical properties of the undoped and Ti-doped α-Fe$_2$O$_3$ films were identical within experimental uncertainty. The optical properties of the Si-doped material were broadly similar to the other films but showed significant differences in the absorption coefficient data (in particular slightly reduced absorption at short wavelengths), probably due to the larger disordered component. Differences in optical properties of crystalline and noncrystalline α-Fe$_2$O$_3$ have been reported.[56] The indirect band gap energies of the three sample
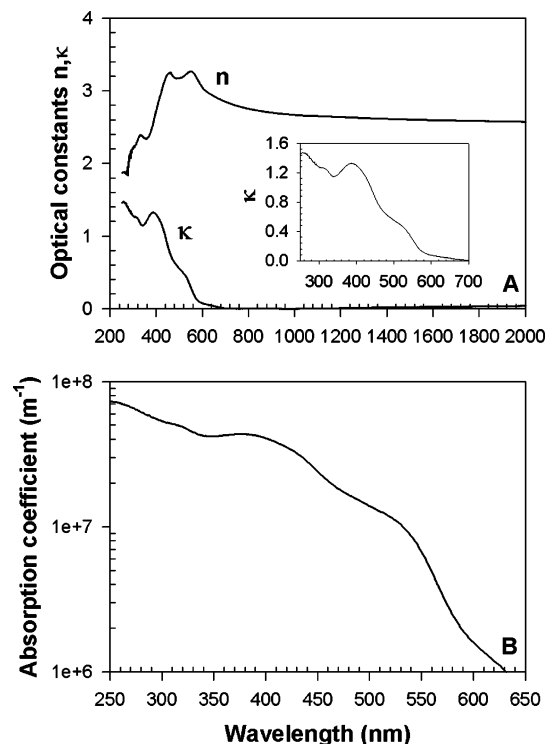
Figure 3. (A) Refractive index (n) and extinction coefficient (κ) and (B) absorption coefficient from reflectance and transmittance measurements of a 120 nm thick Ti-doped α-Fe_2O_3 film versus wavelength.

types calculated from the absorption coefficient of the films deposited on the FTO substrates were all similar (around 1.9 eV). Hence, the improved photocurrent with doping is not due to absorption effects.

Optical transitions have previously been assigned to the features in the extinction coefficient data at approximately 265, 320, 395, 530, and 650 nm.[57,58] The rapid falloff of absorption coefficient with wavelength approaching the band gap value is characteristic of indirect band gap materials such as hematite. It means that a considerable thickness of hematite is required to absorb a large fraction of the radiation at wavelengths approaching the band gap value. Coupled with the short diffusion length in hematite, this highlights the challenge in obtaining high efficiencies at wavelengths approaching the band gap value.

Structural Properties. Figure 4 shows SEM images of the surface microstructure of an FTO conducting glass substrate (A), and an undoped (B), Ti-doped (C) and Si-doped (D) α-Fe_2O_3 film along with their respective cross-sections (E, F, G, and H). In the cross-sectional images of the magnetron sputtered films, three layers are visible. The top layer is the α-Fe_2O_3 film, the middle layer is the FTO, and the bottom layer is the glass substrate. Figure 4E, showing the cross-section of the bare FTO substrate, has only the glass and FTO layers. All of the magnetron sputtered films appear to be dense, with some surface cracking apparent in the undoped and Si-doped films. The cracks may be thermally generated during cooling or annealing. The undoped and Ti-doped α-Fe_2O_3 films have a similar surface microstructure of irregular grains that appear to have a columnar structure from the cross-sectional images. The Si-doped α-Fe_2O_3 film is composed of smaller grains that extend throughout the bulk of the film. Grain sizes of the undoped, Ti-doped, and Si-doped α-Fe_2O_3 films, as estimated from the SEM images of the surfaces, are in the ranges of 75–150, 40–100, and 15–30 nm respectively. Mörl et al.[59] and Miller et al.[38] used reactive sputtering to produce Fe_2O_3 films, and both

observed very similar surface structure to that shown in Figure 4, panels B and C. Mörl et al. also presented cross-sectional images of fractured films showing columnar growth.

Figure 5A shows Raman spectra of a hematite reference (RRUFF ID R050300)[60] compared to those of undoped (B), Ti-doped (C), and Si-doped (D) magnetron sputtered α-Fe_2O_3 films on FTO substrates after annealing. At the excitation wavelength of 514.5 nm, the laser was absorbed to a depth of around 100 nm in the hematite films. Hence, there is no contribution from the substrate in the signal. The spectra of the undoped and Ti-doped films clearly identified hematite as the only phase present and matched the reference spectrum well. The Si-doped α-Fe_2O_3 film exhibited very broad features that appeared to be shifted to higher wavenumbers compared to the reference spectrum. Such behavior is characteristic of a material with very small crystals or a high amorphous content. We observed a very similar Raman spectrum for α-Fe_2O_3 deposited using filtered arc deposition, doped with Si using tetramethylsilane as a precursor.[39] The Raman peak around 660 cm^{-1} has been assigned to disorder in α-Fe_2O_3.[33,46,61,62] The Si-doped and Ti-doped films exhibited a peak at this position, whereas the undoped film did not. Bersani et al.[62] have correlated crystal size with the intensity of the mode around 660 cm^{-1}, suggesting that the mode may be related to surface and grain boundary disorder. The very large disorder peak evident in the Raman spectrum of the Si-doped material is consistent with the presence of significant grain boundary defects. The size of the peak at 660 cm^{-1} reduced after the films were annealed. Peak narrowing was also observed after annealing, indicating enhanced crystallinity.

Figure 6 shows XRD patterns of (A) a hematite reference powder, where the XRD peaks are labeled, and (B) undoped, (C) Ti-doped, and (D) Si-doped magnetron sputtered α-Fe_2O_3 films on FTO substrates after annealing. An expanded view of the major (110) peak of each sample is also shown, where (E) is an as-deposited undoped hematite film. The peaks labeled with an asterisk are tin oxide (casseterite JCPDS 21–1250) from the FTO substrate. The data have been normalized to the major tin oxide peak at $2\theta = 37.8°$, corrected for X-ray attenuation in the hematite film and have been smoothed. The background, containing a broad feature from the amorphous glass substrate centered around $2\theta = 30°$, has been subtracted. All peaks not assigned to tin oxide were identified as hematite (JCPDS 33–0664), with no other iron oxide or impurity phases identified. The XRD patterns are dominated by the scattering from the substrate, with the hematite peaks small in comparison. If the hematite films contain amorphous material (as suggested by the Raman spectra), it is likely that the characteristic broad features expected in the XRD patterns would not be discernible from those of the substrate.

The XRD patterns of the hematite films differed significantly from the hematite reference spectrum. On the whole, the XRD patterns are weak, indicating a low level of crystallinity (particularly in the case of the Si-doped film). Most of the hematite peaks were present for the Ti-doped α-Fe_2O_3 film, but in the case of the undoped and Si-doped α-Fe_2O_3 films, only the (110) and (300) peaks were visible. If other peaks are present, they are very small. The undoped film showed a very strong (110) peak compared to the other films. Both the (110) and (300) peaks for the Si-doped film were very weak. The relative intensities of the XRD peaks compared to that of the reference spectrum suggest that all three film-types are preferentially orientated. If the films had a random crystallographic orientation, then the major hematite peaks (104) and (110) would
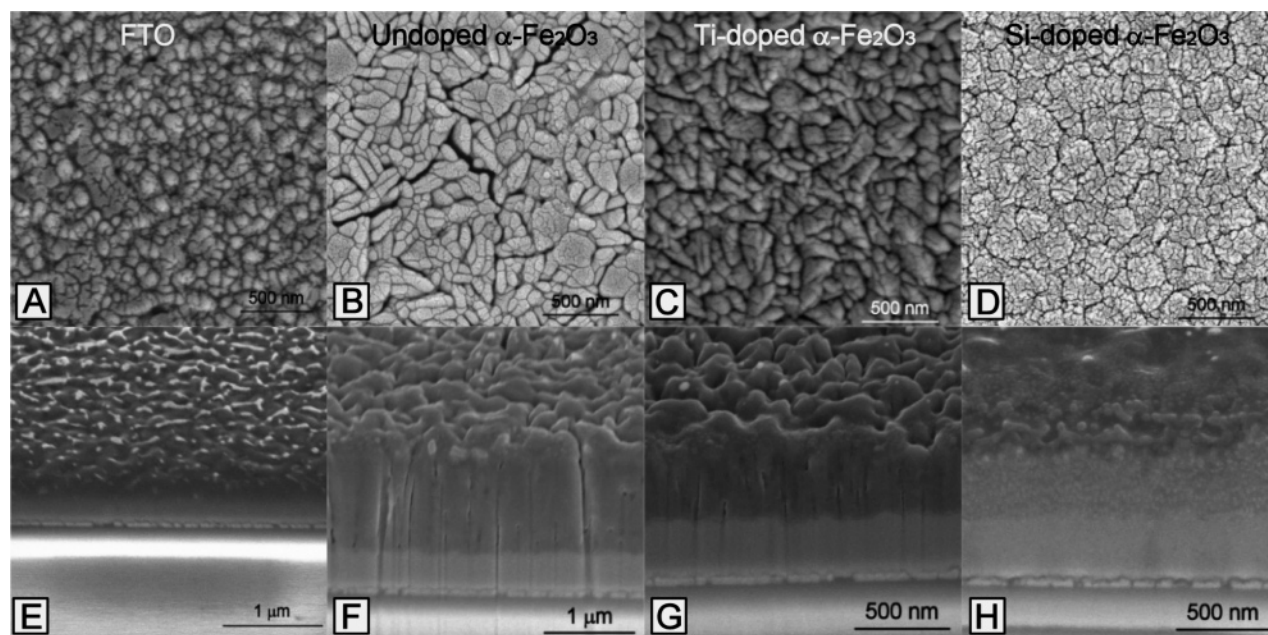
Enhanced Hydrogen Production from Doped Hematite

J. Phys. Chem. C, Vol. 111, No. 44, 2007 **16483**

Figure 4. SEM images of (A) an uncoated FTO substrate, (B) undoped, (C) Ti-doped, and (D) Si-doped α-Fe2O3 films, and their respective cross-sections (E−H).
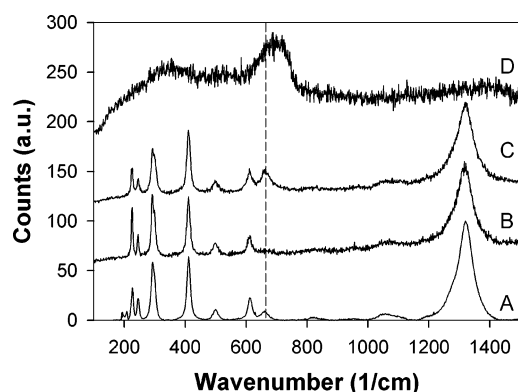

Figure 5. Raman spectra of a (A) hematite reference compared to that of (B) undoped, (C) Ti-doped, and (D) Si-doped α-Fe$_2$O$_3$ films on FTO substrates after annealing.

Figure 6. XRD patterns of (A) hematite reference powder, where the XRD peaks are labeled and (B) a 265 nm thick undoped, (C) a 550 nm thick Ti-doped, (D) a 755 nm thick Si-doped magnetron sputtered α-Fe$_2$O$_3$ films on FTO substrates after annealing, and (E) an as-deposited 265 nm thick undoped α-Fe$_2$O$_3$ film. The asterisks denote peaks from the FTO substrate. The peak heights have been normalized to the major FTO peak and corrected for X-ray attenuation in the film. An expanded view of the major (110) peak of each sample is also shown.

be very strong, and minor peaks such as the (300) would be weak. The fact that the (104) peak is observed as a weak peak (only for the Ti-doped material) and that the (300) peak is a major peak for all samples indicates preferred orientation. The strong orientation of the (110) and (300) directions indicate that the *c* axis of the hexagonal hematite unit cell is aligned parallel to the substrate (or the basal planes are aligned perpendicular to the substrate). The hematite peak positions of the Ti-doped α-Fe$_2$O$_3$ film are shifted to higher angles compared to the reference spectrum. The magnitude of the shift increases with angle, consistent with a decrease in the lattice parameters. The FTO peak positions have not changed, indicating that the shift is not an artifact of the measurement. Crystal sizes calculated using the Scherrer equation from the full-width-half-maximum values of the (110) peaks in the XRD patterns of the undoped, Ti-doped, and Si-doped α-Fe$_2$O$_3$ films were around 65, 40, and 20 nm respectively. An expanded view of this peak for the three sample types is shown in Figure 6 where pattern (E) is that of an as-deposited undoped α-Fe$_2$O$_3$ film. A large increase in the intensity of the (110) (and other) peaks is observed after annealing (Figure 6B), along with an increase in the crystal size from 50 to 65 nm, indicating enhanced crystallinity. Here crystals are defined as the area of local order for diffraction
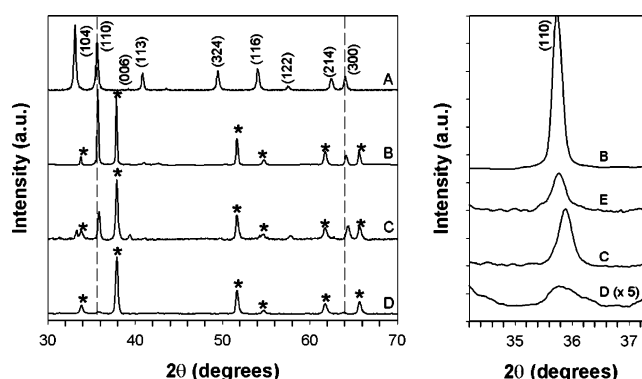
purposes. Grains may be single crystals or comprised of a number of crystals of the same or similar crystallographic orientation. Hence the grain size as determined from observation of SEM images may not be the same as the crystal size determined by XRD.

The broad features evident in the XRD and Raman spectra of the Si-doped α-Fe$_2$O$_3$ suggest that the material may not be fully crystalline. Additional annealing treatments (up to 165 h at 550 °C) of the Si-doped material were undertaken in an attempt to increase the film crystallinity. No change in the photoelectrochemical performance or the XRD pattern or Raman spectra of the film was observed after the extended annealing. The annealing temperature was limited to 550 °C due to the FTO conducting glass substrate and may not have been high enough to produce significant crystal growth.

The XRD patterns of the films deposited at a lower deposition rate showed a narrowing of the diffraction peaks indicating larger crystals. The crystal sizes of the Ti-doped and Si-doped
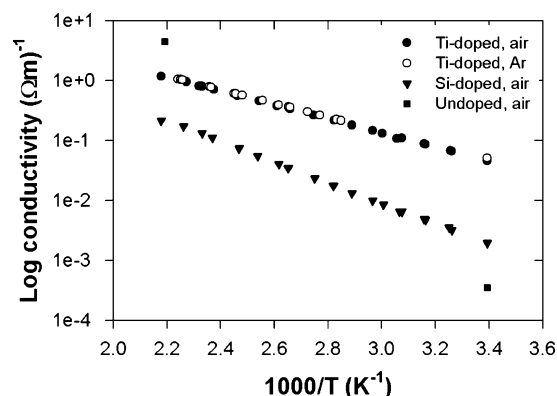
Figure 7. Log conductivity as a function of inverse temperature of doped and undoped α-Fe_2O_3 films measured in air and argon atmospheres.

α-Fe_2O_3 films increased from 40 to 50 nm and from 20 to 30 nm, respectively. The Ti-doped film was more strongly oriented, with a 2.5 times increase in the relative magnitude of the (110) peak observed. No change in the Raman spectra was observed when the films were deposited at a lower rate.

Electrical Properties. Initial measurement of the room-temperature conductivity (after the samples had been annealed at 550 °C) exhibited values of 10^{-4}–10^{-5} Ω^{-1} m^{-1} for all samples. The conductivity values showed drift over time scales of tens of minutes. The samples were then heated to determine the temperature dependence of the conductivity. The conductivity behavior changed to a regime exhibiting much higher conductivity values, during heating (to less than 180 °C, under either argon or air). Upon cooling, the results presented in Figure 7 were obtained. The lower conductivity state could be reproduced by annealing the films again at 550 °C. Further heating to lower temperatures re-established the higher conductivity behavior shown in Figure 7. Hence, although the results shown in Figure 7 were reproducible, we do not understand the existence of a lower conductivity state induced by annealing at 550 °C.

Ohmic behavior was observed for the Si-doped and Ti-doped α-Fe_2O_3 films. However ohmic behavior could not be achieved with the undoped sample despite the use of a number of different contact materials in addition to the FTO contacts. The undoped α-Fe_2O_3 conductivity values plotted in Figure 7 were consequently derived from the linear region of the differential conductance determined at high applied voltages from the current–voltage curves of the sample. The back contact of the undoped sample may not have been ohmic, thus collection of electrons may have been impeded. To check this, an undoped sample was identically prepared on a Ti metal substrate. This sample showed no improvement in photocurrent, whereas the native TiO_2 layer formed during preparation worked well alone.

The conductivity curves of the Ti-doped sample measured (as discussed above) in air and argon atmospheres are similar implying that absorption of water vapor was not an important factor. Activation energies, E_a, have been calculated from the gradients of linear fits to the data shown in Figure 7. These values are listed along with the room-temperature conductivity values of the undoped, Si-doped, and Ti-doped α-Fe_2O_3 films in Table 2. Given that the conductivity of the undoped sample was determined using a different method to that for the doped samples, it may not be appropriate to directly compare the data. This being said, the conductivity values do suggest that doping with both Si and Ti increases the conductivity of hematite at room temperature, as expected from the results of previous

studies.[21,23,26] The conductivity of the Ti-doped film is more than 1 order of magnitude higher than that of the Si-doped film at room temperature. The activation energy of the Ti-doped α-Fe_2O_3 is lower than that of the Si-doped film.

The undoped material in this study showed a similar room-temperature conductivity value to that often quoted for high-purity α-Fe_2O_3 ($<10^{-4}$ Ω^{-1} m^{-1}).[23,63] Miller et al.[64] observed a room-temperature conductivity of around 10^{-4} Ω^{-1} cm^{-1} for undoped magnetron sputtered α-Fe_2O_3. Their samples deposited at lower oxygen partial pressure showed higher conductivity values, which was attributed to reduced grain boundary scattering as a result of an increase in crystal size. The conductivity of the Ti-doped hematite is around 3 orders of magnitude lower than values quoted in the literature for 1–2% Ti-doped material,[24,28] whereas the conductivity of the Si-doped α-Fe_2O_3 is around 2 orders of magnitude higher than the largest of a range of values[63,65] quoted for 2 mol % Ge-doped hematite (where Ge is considered as an analogous dopant to Si). A wide range of conductivity values have been reported for hematite in the literature as the conductivity is highly dependent on the concentration and type of impurity. Jonker and van Houten[27] commented that the concentration of impurity ions required to increase the conductivity of α-Fe_2O_3 significantly is large, and hence, impurities concentrations as high as 0.1% are often of little importance. However, the addition of very small amounts of some impurities has been shown to have a significant effect on the electrical and photoelectrochemical performance.[17,24] Morin[26] observed a small change in conductivity with the addition of 0.05% Ti, whereas de Cogan and Lonergan[24] reported a much larger increase in conductivity with the addition of 0.01% Ti.

Examples of the electrochemical impedance spectroscopy data measured at −0.5V vs SCE are shown in Figure 8 in the form of Nyquist plots (A−C) and Mott−Schottky plots determined from the fitted space charge layer capacitance values at each potential (D−F) for the undoped, Si-doped and Ti-doped α-Fe_2O_3 films, respectively. Carrier concentration (N_D) and flat-band potential (V_{fb}) values calculated from the impedance spectroscopy data are shown in Table 2, along with mobility values calculated from the room-temperature conductivities and carrier concentrations. The lesser gradient of the Mott−Schottky curves in the high potential region seen in Figure 7, panels D and E, has been observed in previous studies and ascribed to a number of possible factors ranging from spatial variation in the donor concentration to the influence of the Helmholz layer.[66,67] The carrier concentration of the Ti-doped material is over 1 order of magnitude higher than that of the Si-doped α-Fe_2O_3. The electron mobilities of the doped films are similar, of the order of 10^{-9} m^2 s^{-1} V^{-1}, which are smaller than mobility values for Ti-doped hematite of the order of 10^{-6} and 10^{-7} m^2 s^{-1} V^{-1} presented by Gardner et al.[21] and Morin,[68] respectively, although similar to those calculated theoretically.[30] If the thermally activated hopping mechanism of conduction is assumed for hematite,[28] where electron transport occurs via hopping between Fe^{3+} and Fe^{2+} sites, then similar mobilities for Si-doped and Ti-doped α-Fe_2O_3 may be expected. The flat-band potentials of our Ti-doped and undoped hematite films tended to be more cathodic than those presented previously[11,14,49,69] (as shown in Table 3). Our Si-doped material showed a more anodic flat-band potential than a Ge-doped α-Fe_2O_3 single crystal[63] (where the Ge dopant is considered to be analogous to Si). Sastri et al.[14] observed a cathodic shift in the flat-band potential with Ti-doping, with a maximum occurring at a dopant level of 1.0% Ti.

Enhanced Hydrogen Production from Doped Hematite

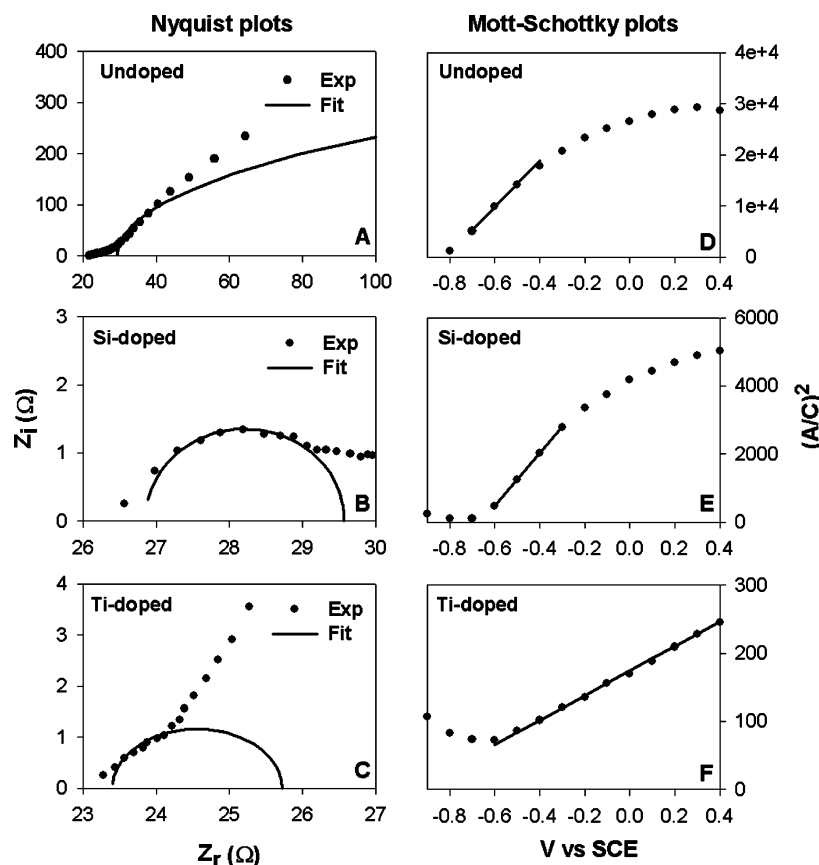*J. Phys. Chem. C, Vol. 111, No. 44, 2007* **16485**

Figure 8. Examples of Nyquist plots showing the imaginary versus the real component of the impedance at -0.5 V vs SCE and modeled impedance, of the (A) undoped (1−10 kHz), (B) Si-doped (5−32 kHz), and (C) Ti-doped (4−25 kHz) α-Fe_2O_3 films (where Z_r and Z_i are the real and imaginary parts of the impedance respectively), and corresponding Mott−Schottky plots for two samples of each material (D−F).

TABLE 3: Flat-Band Potentials for the Magnetron Sputtered α-Fe_2O_3 Films Compared to Literature Values[a]

author	sample	V_{fb} (V/SCE)
this study	undoped	$-0.84^{+0.02}_{-0.07}$
	5% Si	$-0.69^{+0.12}_{-0.00}$
	5% Ti	$-0.99^{+0.20}_{-0.01}$
Sastri et al., 1980[14]	undoped	-0.65
	0.5% Ti	-0.67
	1.0% Ti	-0.8
	1.5% Ti	-0.72
McCann and Badwal, 1982[49]	1.0% Ti	-0.75
Kennedy and Frese, 1977[69]	undoped	-0.73
Dare-Edwards et al., 1983[11]	0.15% Ti	-0.5
Sieber et al., 1985[63]	1.0% Ge	-0.95

[a] All measurements were undertaken in 1 M NaOH electrolyte except those of Kennedy and Frese[69] (2 M NaOH) and Dare-Edwards et al.[11] (1 M KOH).

Figure 9 shows the surface state densities and time constants (shown in Table 2) derived from the residual capacitance not attributed to the space charge layer. Despite the unsophisticated description and assumptions, the measured values are fitted surprisingly well by the two adjustable parameter model (Figure 9A shows examples). The Si-doped film shows the highest concentration of surface states, approximately 1 order of magnitude higher than the Ti-doped film and about 3 orders of magnitude higher than the undoped over most of the voltage range (Figure 9B). Figure 9C shows the Ti-doped film to have the shortest time constants followed by the Si-doped and then undoped films. These differences are likely to be inversely proportional to the capture/emission cross-section since the thermal electron velocity is expected to be constant for all the films.

4. Discussion

It is clear that in the case of our magnetron sputtered α-Fe_2O_3 films doping was necessary to produce photocatalytically active material, with the Ti-doped α-Fe_2O_3 exhibiting a much higher photocurrent than the Si-doped α-Fe_2O_3 at the bias voltages investigated. It is interesting to note that Miller et al.[64] observed significant photocurrents from undoped hematite films produced using a very similar magnetron deposition process. It is surprising that the Si-doped material showed significant photoactivity, given that it appears to be highly amorphous and have a high level of surface disorder. The high photocurrents achieved by Si-doped α-Fe_2O_3 samples prepared by other techniques[16,4] can probably be attributed to their material being more crystalline. Several mechanisms have been proposed for the improvement of the photocatalytic performance of hematite with doping. We discuss these mechanisms in the context of our results and those presented in the literature.

Kay et al.[4] and Cesar et al.[16] attributed good photocatalytic behavior of Si-doped α-Fe_2O_3 produced by CVD and spray pyrolysis techniques respectively, in part, to a high degree of preferential crystallographic orientation. Strong (110) and (300) peaks were observed in the X-ray diffraction patterns, indicating that the basal planes (001) were aligned perpendicular to the substrate. It was suggested that photoelectron collection was enhanced because of the orientation of the strongly conducting basal planes, whereas photohole transfer was facilitated by the short diffusion distances from nanostructure to electrolyte. Bedwell and McCartney[70] measured the photoelectrochemical response of single crystals cut to expose different crystallographic planes to the electrolyte. They found that an electrode exposing the (001) plane showed little photocurrent, but the
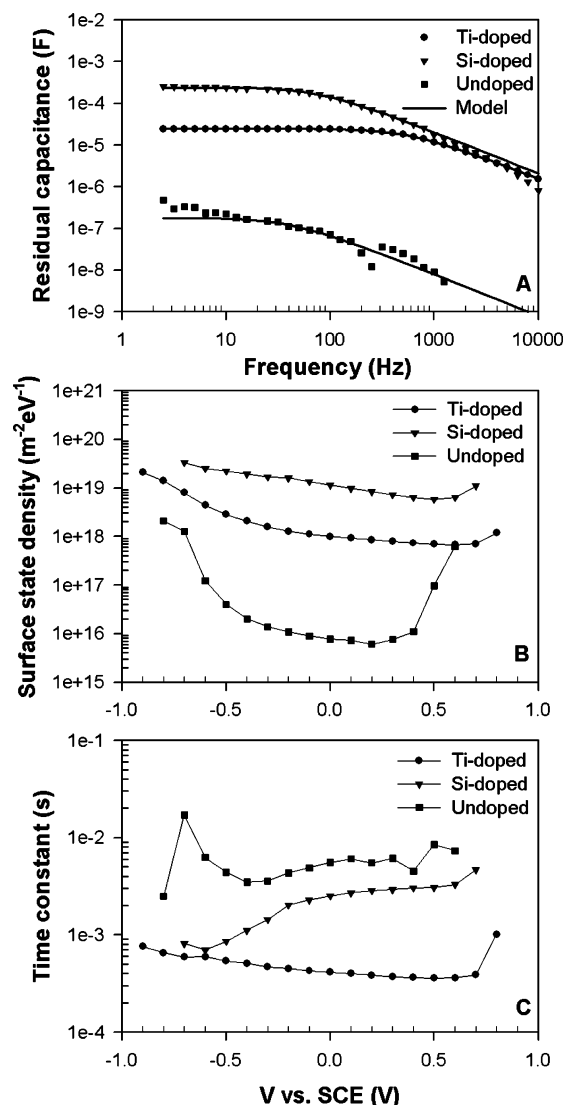
16486 *J. Phys. Chem. C, Vol. 111, No. 44, 2007*

Glasscock et al.

Figure 9. (A) Examples of the residual capacitance as a function of frequency measured at 0.5 V vs SCE and model fitted assuming this capacitance can be attributed to surface states. (B) The surface state density per unit energy determined from the fits shown in (A) at each measured potential. (C) Corresponding surface state emission/capture time constants plotted against potential.

(012) plane showed a good photoresponse. The difference in photocurrent was attributed to the much higher resistivity in the [001] direction ((110) plane) (10^4 Ω m) compared to the [012] direction (20 Ω m). The anisotropic nature of the electrical conductivity of hematite is well-known and has been observed experimentally[71,72] and demonstrated theoretically.[30,73] However, the magnitude of the anisotropy is highly dependent on impurities. In the present study, the doped and undoped films all exhibited a preferred orientation of the basal planes perpendicular to the substrate yet showed very different photocurrents. The Ti-doped α-Fe$_2$O$_3$ deposited at a lower deposition rate showed an increase in the preferred orientation in the [110] direction but no change in photocurrent. Therefore, it appears unlikely that crystallographic orientation is a dominant factor determining the photocatalytic performance of these films.

It is clear that the introduction of Ti and Si dopants affects the growth mechanism of the magnetron sputtered hematite, resulting in films with different crystallinity, alignment, and morphology. The Si appears to prevent the growth of highly crystalline material, whereas the presence of Ti allows crystalline growth. Given the low partial pressure of oxygen during

deposition, it is likely that Fe is deposited onto the substrates and then oxidizes to form α-Fe$_2$O$_3$. The mobility of the Fe atoms will affect the crystal structure and orientation of the oxide. It has been suggested that preferential growth in the [110] direction is due to facile Fe atom diffusion in this direction.[36] It is possible that the Si is reducing the mobility of the Fe atoms during growth, which might restrict the formation of large crystallites.

The Raman spectrum of the Si-doped α-Fe$_2$O$_3$ is strikingly different to the spectra of the Ti-doped and undoped α-Fe$_2$O$_3$, so much so that it would be impossible to identify the Si-doped α-Fe$_2$O$_3$ as hematite without the X-ray diffraction data. In contrast, the XRD patterns of the three materials are broadly similar. However, the XRD peaks of the Si-doped material are small. The Raman technique is probing only the top 100 nm of the film, whereas XRD analyzes the entire film. These results suggest that the bulk material of the doped and undoped films is similar (apart from differences in crystallographic orientation), whereas the near-surface region of the Si-doped α-Fe$_2$O$_3$ is substantially more disordered than that of the Ti-doped and undoped films. Given the smaller grain size of the Si-doped α-Fe$_2$O$_3$ than the undoped or Ti-doped material, the Raman technique would be analyzing a greater number of grains, with a higher surface/grain boundary contribution. The magnitude of the Raman disorder peak from the Si-doped film is considerably larger than that of the Ti-doped film, consistent with the higher calculated surface state density for the Si-doped α-Fe$_2$O$_3$. The surface state density of the undoped α-Fe$_2$O$_3$ film was orders of magnitude lower than that of the doped materials and did not exhibit the disorder peak in its Raman spectrum. These results support the suggestion by Bersani et al.[62] that this Raman peak is related to surface and/or grain boundary disorder.

The IPCE values of the magnetron sputtered films are broadly similar to those presented by others (see Figure 1); however, due to the high onset potentials of our films, a more positive bias voltage is required (which will limit the photoconversion efficiency). The performance of our hematite electrodes is still well below the maximum theoretically achievable for a semiconductor with a band gap around 2 eV. The onset potentials of the hematite films are far from the respective flat-band potentials. This has been linked to surface recombination and may be inherently linked to very slow transfer of Fe^{4+} ions (holes) to the electrolyte, since there is an energy mismatch between the holes in the Fe d orbitals and the p orbitals of the hydroxide bonded to the oxygen sites on the surface.[11] Hence, a build-up of positive charge at the surface perturbs the space-charge layer and enhances recombination processes. It has been suggested that it is only the O 2p holes that are active in the water splitting reaction.[8] The larger onset potential and flat-band potential of the Si-doped α-Fe$_2$O$_3$ compared to the Ti-doped α-Fe$_2$O$_3$ may be explained by the presence of amorphous (disordered) material at the surface. The slow increase in the onset current evident from the photocurrent−voltage curves of all three sample types has also been attributed to recombination.[74] Surface treatment with Co[4] and KI[18] have been shown to increase the photocurrent from doped α-Fe$_2$O$_3$ films. Our surface modification experiments, where very thin films of TiO$_2$ or Ti-doped α-Fe$_2$O$_3$ were deposited onto undoped hematite, showed no improvement in the generated photocurrent. If the undoped material did indeed have a highly defective surface layer, then perhaps the addition of a Ti-containing layer would not be expected to solve the surface transfer problems. Differences in the crystal structure between the films and the fact that Ti is a very good oxygen getter (and may be reducing the hematite film) may also have affected the results.

Enhanced Hydrogen Production from Doped Hematite

J. Phys. Chem. C, Vol. 111, No. 44, 2007 **16487**

The concentration of charge carriers in the Ti-doped α-Fe_2O_3 is over 1 order of magnitude larger than that of the Si-doped material. We would expect lower carrier concentrations to correspond to wider depletion layers at the electrolyte interface, thus leading to a greater harvesting of charge carriers. However, a Schottky barrier model predicts that the transit time through the depletion layer varies as the square of the Debye length (inversely with charge carrier concentration), so that the greater harvesting of charge carriers may be offset by increased recombination.

The activation energy for electrical conductivity of the hematite thin films was reduced by the introduction of Ti or Si. This suggests a change to the bulk properties of the material, rather than just a surface effect. The undoped α-Fe_2O_3 showed a high activation energy around 0.7 V, which is a similar value to that obtained for undoped hematite produced by filtered arc deposition.[46] Gardner et al.[20] observed an activation energy of 0.7 eV from undoped polycrystalline hematite, which was attributed to the formation of other iron oxide phases (such as Fe_3O_4) at grain boundaries. The narrow band gap of sub-oxide phases such as Fe_3O_4 would allow recombination pathways for photoholes. Much lower activation energy values ($\sim$0.1 eV) were observed in regions where complete grain boundary oxidation was thought to occur, similar to values theoretically calculated values for hematite.[27] Miller et al.[64] also reported a reduction in activation energy values with increasing crystal size. The Ti or Si impurities added to the hematite films may segregate between the grains, passivating recombination at the grain boundaries. This would be expected to increase carrier lifetimes and consequently hole diffusion lengths. This argument is consistent with the results of Kay et al.,[4] who showed that a thin SiO_2 layer at the base of their nanostructured photoelectrodes led to an improvement in performance. However, if grain boundary recombination was the rate-limiting step for hematite electrodes, then it would be expected that single crystals would perform better than polycrystalline material, which is not generally true (see Figure 1). It is clear that α-Fe_2O_3 needs to be highly crystalline in order to produce a high photocurrent. However, we believe that surface recombination is likely to be the dominant factor limiting the performance of our hematite thin films, rather than recombination at grain boundaries.

5. Conclusions

We have presented an extensive study of the photoelectrochemical, electrical, structural, and optical properties of doped and undoped α-Fe_2O_3 films fabricated using magnetron-sputtering. It was observed that doping was necessary to achieve significant photoelectrochemical activity. The crystallographic orientation of the films does not appear to be a dominant factor affecting the photocurrent, and also the reduced ohmic drop due to the change in conductivity with doping is insufficient to explain the observed changes in the photoelectrochemical activity. The undoped hematite is thought to have poor performance due to short diffusion lengths of charge carriers and/or poor surface charge transfer. The proposed mechanism for the enhanced photocurrent with doping is an improvement of the transfer rate coefficient at the surface and possibly also passivation of the grain boundaries by the dopants. The Si-doped hematite is thought to work less well than the Ti-doped material as the Si impurity appears to promote smaller grains and have a high level of surface states, enhancing recombination at the surface and at grain boundaries. Further work will involve modification of the surface of the hematite films in an attempt to increase the charge-transfer coefficient. An interesting observation from this study is that the barrier model traditionally used to describe semiconductor charge transfer does not fit our IPCE data well. This issue will be investigated further as it may provide insight into charge-transfer processes in hematite that are not currently well-understood. This may have implications for the further development of thin films and nanostructured films of α-Fe_2O_3 for water splitting applications.

References and Notes

(1) Nowotny, J.; Sorrell, C. C.; Sheppard, L. R.; Bak, T. *Int. J. Hydrogen Energy* **2005**, *30* (5), 521−544.

(2) Bolton, J. R. *Solar Energy* **1996**, *57* (1), 37−50.

(3) Murphy, A. B.; Barnes, P. R. F.; Randeniya, L. K.; Plumb, I. C.; Grey, I. E.; Horne, M. D.; Glasscock, J. A. *Int. J. Hydrogen Energy* **2006**, *31* (14), 1999−2017.

(4) Kay, A.; Cesar, I.; Grätzel, M. *J. Am. Chem. Soc.* **2006**, *128* (49), 15714−15721.

(5) Lindgren, T.; Vayssieres, L.; Wang, H.; Lindquist, S.-E. *Chemical Physics of Nanostructured Semiconductors*; Kokorin, A. I., Bahnemann, D. W., Eds.; VSP: Boston, 2003; pp 83−110.

(6) Miller, E. L.; Paluselli, D.; Marsen, B.; Rocheleau, R. E. *Solar Energy Mater. Solar Cells* **2005**, *88* (2), 131−144.

(7) Aroutiounian, V. M.; Arakelyan, V. M.; Shahnazaryan, G. E.; Stepanyan, G. M.; Khachaturyan, E. A.; Wang, H. T. J. *Solar Energy* **2006**, *80* (9), 1098−1111.

(8) Ingler, W. B.; Khan, S. U. M. *Electrochem. Solid State Lett.* **2006**, *9* (4), G144−G146.

(9) Jorand Sartoretti, C.; Alexander, B. D.; Solarska, R.; Rutkowska, I. A.; Augustynski, J.; Cerny, R. *J. Phys. Chem. B* **2005**, *109* (28), 13685−13692.

(10) Kennedy, J. H.; Frese, K. W., Jr. *J. Electrochem. Soc.* **1978**, *125* (5), 709−714.

(11) Dare-Edwards, M.; Goodenough, J. B.; Hamnett, A.; Trevellick, P. R. *J. Chem. Soc., Faraday Trans. 1* **1983**, *79*, 2027−2041.

(12) Bak, T.; Nowotny, J.; Rekas, M.; Sorrell, C. C. *Int. J. Hydrogen Energy* **2002**, *27* (10), 991−1022.

(13) Shinar, R.; Kennedy, J. H. *Solar Energy Mater.* **1982**, *6*, 323−335.

(14) Sastri, M. V. C.; Nagasubramian, G. *Proceedings of the 3rd World Hydrogen Energy Conference;* Hydrogen Energy Progress, 1980.

(15) Fredlein, R. A.; Bard, A. J. *J. Electrochem. Soc.* **1979,** *126* (11), 1892−1898.

(16) Cesar, I.; Kay, A.; Gonzalez, Martinez, J. A.; Grätzel, M. *J. Am. Chem. Soc.* **2006**, *128* (14), 4582−4583.

(17) Kennedy, J. H.; Anderman, M.; Shinar, R. *J. Electrochem. Soc.* **1981**, *128* (11), 2371−2373.

(18) Kennedy, J. H.; Shinar, R.; Ziegler, J. P. *J. Electrochem. Soc.* **1980**, *127* (10), 2307−2309.

(19) Turner, J. E.; Hendewerk, M.; Parmeter, J.; Neiman, D.; Somorjai, G. A. *J. Electrochem. Soc.* **1984**, *131* (8), 1777−1783.

(20) Gardner, R. F. G.; Sweett, F.; Tanner, D. W. *J. Phys. Chem. Solids* **1963**, *24*, 1183−1196.

(21) Gardner, R. F. G.; Sweett, F.; Tanner, D. W. *J. Phys. Chem. Solids* **1963**, *24*, 1175−1181.

(22) Morin, F. J. *Phys. Rev.* **1950**, *78*, 819−820.

(23) Warnes, B. F.; Aplan, F. F.; Simkovich, G. *Solid State Ionics* **1984**, *12*, 271−276.

(24) de Cogan, D.; Lonergan, G. A. *Solid State Commun.* **1974**, *15*, 1517−1519.

(25) Merchant, P.; Collins, R.; Kershaw, R.; Dwight, K.; Wold, A. *J. Solid State Chem.* **1979**, *27*, 307−315.

(26) Morin, F. J. *Phys. Rev.* **1951**, *83* (5), 1005−1010.

(27) Jonker, G. H.; van Houten, S. *Halbleiterprobleme* **1961**, *6*, 118−150.

(28) Bosman, A. J.; van Daal, H. J. *Adv. Phys.* **1970**, *19* (77), 1−117.

(29) Gharibi, E.; Hbika, A.; Dupre, B.; Gleitzer, C. *Eur. J. Solid State Inorg. Chem.* **1990**, *27*, 647−658.

(30) Iordanova, N.; Dupuis, M.; Rosso, K. M. *J. Chem. Phys.* **2005**, *122* (14), 144305−1, 144305−10.

(31) Beermann, N.; Vayssieres, L.; Lindquist, S.-E.; Hagfelt, A. *J. Electrochem. Soc.* **2000**, *147* (7), 2456−2461.

(32) Lindgren, T.; Wang, H.; Beermann, N.; Vayssieres, L.; Hagfeldt, A.; Lindquist, S.-E. *Solar Energy Mater. Solar Cells* **2002**, *71* (2), 231−243.

(33) Fu, Y. Y.; Wang, R. M.; Xu, J.; Chen, J.; Yan, Y.; Narlikar, A. V.; Zhang, H. *Chem. Phys. Lett.* **2003**, *379*, 373−379.

(34) Kim, C. H.; Chun, H. J.; Kim, D. S.; Kim, S. Y.; Park, J.; Moon, J. Y.; Lee, G.; Yoon, J.; Jo, Y.; Jung, M.-H.; Jung, S.; Lee, C. J. *Appl. Phys. Lett.* **2006**, *89* (22), 223103−1, 223103−3.

(35) Wang, R.; Chen, Y.; Fu, Y.; Zhang, H.; Kisielowski, C. *J. Phys. Chem. B* **2005**, *109* (25), 12245−12249.

(36) Wen, X. G.; Wang, S. H.; Ding, Y.; Wang, Z. L.; Yang, S. H. *J. Phys. Chem B* **2005**, *109* (1), 215−220.

(37) Xu, Y. Y.; Rui, X. F.; Fu, Y. Y. Z. H. *Chem. Phys. Lett.* **2005**, *410* (1−3), 36−38.

(38) Miller, E. L.; Rocheleau, R. E.; Khan, S. *Int. J. Hydrogen Energy* **2004**, *29* (9), 907−914.

(39) Glasscock, J. A.; Barnes, P. R. F.; Plumb, I. C.; Bendavid, A.; Martin, P. J. *Proc. SPIE* **2006**, *6430*, N1−N12.

(40) Duret, A.; Grätzel, M. *J. Phys. Chem. B* **2005**, *109* (36), 17184−17191.

(41) Khan, S. U. M.; Akikusa, J. *J. Phys. Chem. B* **1999**, *103* (34), 7184−7189.

(42) Sanchez, C.; Sieber, K. D.; Somorjai, G. A. *J. Electroanal. Chem.* **1988**, *252* (2), 269−290.

(43) Savvides, N. *J. Appl. Phys.* **1984**, *55*, 4232−4238.

(44) Poelman, D.; Smet, P. *J. Phys. D: Appl. Phys.* **2003**, *36* (15), 1850−1857.

(45) Szczyrbowski, J. *J. Phys. D: Appl. Phys.* **1978**, *11*, 583.

(46) Glasscock, J. A.; Barnes, P. R. F.; Plumb, I. C.; Bendavid, A.; Martin, P. J. *Thin Solid Films* **2007**, in press.

(47) Aroutiounian, V. M.; Arakelyan, V. M.; Shahnazaryan, G. E.; Stepanyan, G. M.; Turner, J. A.; Kocha, S. S. *Electrochim. Acta* **2000**, *45* (12), 1999−2005.

(48) Bockris, J. O.; Reddy, A. K. N. *Modern Electrochemistry: Electrodics in Chemistry, Engineering, Biology and Environmental Science*; Kluwer Academic/Plenum Publishers: New York, 2000.

(49) McCann, J. F.; Badwal, S. P. S. *J. Electrochem. Soc.* **1982**, *129* (3), 551−559.

(50) Özdemir, A. F.; Türüt, A.; Kokçe, A. *Thin Solid Films* **2003**, *425* (1−2), 210−215.

(51) *MOS Physics and Technology*; Nicolian, E. H., Brews, J. R., Eds.; Wiley: New York, 1982.

(52) Barnes, P. R. F.; Randeniya, L. K.; Vohralik, P. F.; Plumb, I. C. *J. Electrochem. Soc.* **2007**, *154* (3), H249−H257.

(53) Butler, M. A. *J. Appl. Phys.* **1977**, *48* (5), 1914−1920.

(54) Harris, L. A.; Gerstner, M. E.; Wilson, R. H. *J. Electrochem. Soc.* **1979**, *126* (5), 850−855.

(55) Maruska, H. P.; Ghosh, A. K. *Solar Energy* **1978**, *20*, 443−458.

(56) Akl, A. A. *Appl. Surf. Sci.* **2004**, *233* (1−4), 307−319.

(57) Marusak, L.; Messier, R.; White, W. *J. Phys. Chem. Solids* **1980**, *41*, 981−984.

(58) Sherman, D. M.; Waite, T. D. *Am. Mineral.* **1985**, *70*, 1262−1269.

(59) Mörl, K.; Röpke, U.; Knappe, B.; Lehmann, J.; Perthel, R.; Schröder, H. *Thin Solid Films* **1979**, *60*, 49−53.

(60) Laetsch, T.; Downs, R. T. *19th General Meeting of the International Mineralogical Association;* Kobe, Japan, 2006.

(61) Pérez León, C.; Kado, L.; Zhang, M.; Müller, A. H. E. *J. Raman Spectrosc.* **2004**, *35*, 165−169.

(62) Bersani, D.; Lottici, P. P.; Montenero, A. *J. Raman Spectrosc.* **1999**, *30*, 355−360.

(63) Sieber, K. D.; Sanchez, C.; Turner, J. E.; Somorjai, G. A. *J. Chem. Soc., Faraday Trans. 1* **1985**, *81*, 1263−1274.

(64) Miller, E. L.; Paluselli, D.; Marsen, B.; Rocheleau, R. E. *Thin Solid Films* **2004**, *466* (1−2), 307−313.

(65) Sanchez, H. L.; Steinfink, H.; White, H. S. *J. Solid State Chem.* **1982**, *41* (1), 90−96.

(66) Anderman, M.; Kennedy, J. H. *Semiconductor Electrodes,* Elsevier: Amsterdam, 1988.

(67) Finklea, H. O. *Semiconductor Electrodes*; Elsevier: Amsterdam, 1988.

(68) Morin, F. J. *Phys. Rev.* **1954**, *93*, No. 6.

(69) Kennedy, J. H.; Frese, K. W. *Electrode Materials and Processes for Energy Conversion and Storage*; The Electrochemical Society Softbound Proceedings Series: Princeton, NJ, 1977.

(70) Bedwell, I. R.; McCartney, E. R. *Mater. Sci. Monogr.* **1980**, *6*, 1159−1172.

(71) Nakau, T. *J. Phys. Soc. Jpn.* **1960**, *15*, 727.

(72) Benjelloun, D.; Bonnet, J.-P.; Doumerc, J.-P.; Launay, J.-C.; Onillon, M.; Hagenmuller, P. *Mater. Chem. Phys.* **1984**, *10*, 503−518.

(73) Kerisit, S.; Rosso, K. *Geochim. Cosmochim. Acta* **2006**, *70* (8), 1888−1903.

(74) Wilson, R. H. *J. Appl. Phys.* **1977**, *48* (10), 4292−4297.